THE INSTANTANEOUS STRUCTURE OF TURBULENT BOUNDARY LAYERS OVER SURFACES WITH SPANWISE HETEROGENEITY

D. D. Wangsawijaya[1]**, C. M. de Silva**[1,2]**, R. Baidya**[1,3]**, D. Chung**[1]**, I. Marusic**[1]**, and N. Hutchins**[1]

[1] Department of Mechanical Engineering, University of Melbourne, VIC 3010, Australia

[2] School of Mechanical and Manufacturing Engineering, University of New South Wales, NSW 2052, Australia

[3] Institute of Fluid Mechanics and Aerodynamics, Universität der Bundeswehr München,
Werner-Heisenberg-Weg 39, 85577 Neubiberg, Germany
d.wangsawijaya@student.unimelb.edu.au

ABSTRACT

Turbulent flows over surfaces with extensive roughness variation in the spanwise direction induce a secondary flow in the form of streamwise aligned counter-rotating vortices. In this study, we conduct cross-plane stereoscopic particle image velocimetry (SPIV) measurements over surfaces constructed from spanwise-alternating smooth and rough strips to emulate spanwise heterogeneity in a rough-walled surface. The half-spanwise-wavelength of the alternating rough and smooth strips S varies from $S/\overline{\delta} = 0.32$–$3.63$, relative to the spanwise-averaged boundary layer thickness, $\overline{\delta}$. Two limiting cases are observed when $S/\overline{\delta} \gg 1$ and $\ll 1$, where the size of secondary flow is limited by $\overline{\delta}$ and S, respectively. Consequently, the regions away from the secondary flow scale according to their local shear stress when $S/\overline{\delta} \gg 1$ and become spanwise homogeneous when $S/\overline{\delta} \ll 1$. We observe that when $S/\overline{\delta} \approx 1$, the secondary flow is particularly strong and appears to fill the entire wall-normal extent of the boundary layer. In this condition, we observe that the spanwise location of the secondary flow is highly time-dependent.

INTRODUCTION

In nature and engineering applications, wall-bounded turbulent flows rarely occur over a smooth surface. More often, the surface has some degree of roughness which causes its behaviour to depart from that of a canonical smooth wall boundary layer. Tools that are available to analyse the behaviour of turbulent boundary layers over rough surfaces, such as the Moody chart (Moody, 1944) and Hama roughness function (Hama, 1954), are based on the assumption that the roughness is homogeneously distributed over the wetted surface. In most cases, however, the surface roughness is heterogeneous. A specific case exists where the roughness properties vary along the spanwise direction. For such a surface, spanwise variations in turbulence induce secondary flows in the form of counter-rotating roll modes over the surface (Hinze, 1967).

A recent study on spanwise heterogeneous roughness by Yang & Anderson (2018), where heterogeneity is imposed through substantially elevated roughness elements above a smooth surface, showed the importance of the spanwise wavelength of the heterogeneous roughness within a range of S/δ, where S is the spanwise spacing between

Table 1. Summary of test cases.

Case	S	$\overline{\delta}$	$S/\overline{\delta}$	$Re_{\overline{\delta}}$	$Re_{\overline{\theta}}$
	(mm)	(mm)		($\times 10^4$)	
SR250	250	69	3.63	6.72	9090
SR160	160	70	2.28	6.84	9200
SR100	100	74	1.35	7.27	10150
SR50	50	81	0.62	7.92	10220
SR25	25	78	0.32	7.49	9990
Ref.	S	δ_s	S/δ_s	Re_{δ_s}	Re_{θ_s}
	(mm)	(mm)		$\times 10^{-4}$	
SW	0	56	0	5.62	7320

roughness elements and δ is the channel half-height. A reversal in the direction of the secondary flows was observed when $S/\delta \approx 1$. Another study by Chung et al. (2018) also confirmed the dependency of the secondary flows on S/δ. Here, the spanwise heterogeneity is imposed through high-low shear stress variation and S is the spanwise width of the high or low stress strip. The results showed that when S/δ is either very small or very large, the roll modes are confined by either S or δ and the regions away from the roll modes induced by the secondary flows show signs of outer layer similarity.

Between the two limiting cases when $S/\delta \approx 1$, the roll modes appear to fill the entire boundary layer and the surface is fully spanwise heterogeneous. Within this range, Nugroho et al. (2013) and Medjnoun et al. (2018) observed a highly energized mode in the 1-D streamwise energy spectra located in the outer layer over C-D riblets and ridge-type roughness, respectively. Through an examination of streamwise velocity fluctuation field over C-D riblets, Kevin et al. (2017) observed a strong flapping of the low-speed structure in the spanwise direction. These findings suggest that the roll modes are not stationary in time. Furthermore, it is also unclear whether this time-varying behaviour of the secondary flow, observed at $S/\delta \approx 1$, extends to the limiting cases where $S/\delta \ll 1$ or $\gg 1$.

In this study, we examine the behaviour of the secondary flow instantaneously over spanwise heterogeneity at various $S/\overline{\delta}$ using the velocity fields captured by cross-plane SPIV experiments.
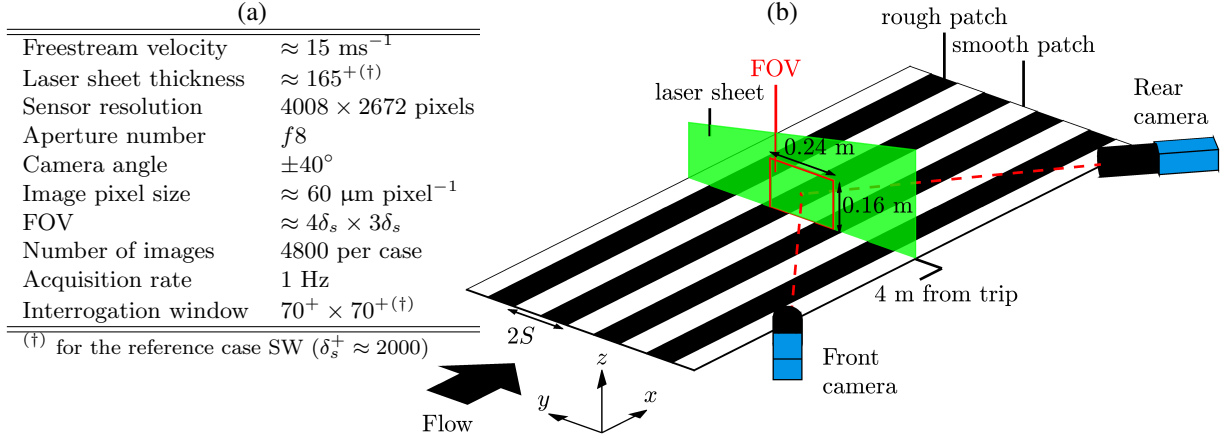
(a)

Freestream velocity	≈ 15 ms^{-1}
Laser sheet thickness	$\approx 165^{+\,(\dagger)}$
Sensor resolution	4008×2672 pixels
Aperture number	$f8$
Camera angle	$\pm 40°$
Image pixel size	≈ 60 µm pixel^{-1}
FOV	$\approx 4\delta_s \times 3\delta_s$
Number of images	4800 per case
Acquisition rate	1 Hz
Interrogation window	$70^+ \times 70^{+\,(\dagger)}$

$^{(\dagger)}$ for the reference case SW ($\delta_s^+ \approx 2000$)

Figure 1. (a) Parameters of the SPIV experiments; (b) Schematic of spanwise heterogeneous roughness model and cross-plane SPIV experiment. The white and black patches correspond to strips of cardboard and sandpaper, respectively. Red box illustrates the field of view captured by the cameras. Laser illumination is provided from the left.

EXPERIMENTAL SETUP

Non-time resolved cross-plane SPIV experiments are performed in a zero pressure gradient, open return boundary layer wind tunnel in the Walter Basset Aerodynamic Laboratory at the University of Melbourne. The test section has the dimension of 6.7 m × 0.94 m × 0.38 m. The spanwise heterogeneous roughness surface covers a 5.6 m-long section of this tunnel, measured from the turbulent boundary layer trip. The measurement plane for the SPIV experiments is located 4 m downstream from the trip.

The spanwise heterogeneous roughness is constructed from spanwise-alternating strips of P-36 grit sandpaper for the rough patch and cardboard for the smooth of equal half-wavelength width S, as shown in figure 1(b). The thickness of the cardboard strips (2 mm thick) is chosen to minimize the variation in the effective virtual origin between rough and smooth strips. The shift in virtual origin is estimated at 0.73 mm or $0.013\delta_s$, measured from the average height difference between the sandpaper strip and the cardboard. Five such surfaces with varying S, detailed in table 1, are constructed in the range of $S/\overline{\delta} = 0.32$–3.63. S is normalized by the spanwise-averaged 98% boundary layer thickness $\overline{\delta}$ for each case. The variation of the boundary layer thickness across the span $\delta(y)$ is shown for selected cases in figure 2, and is within $\pm 20\%$ for all cases tested here. A reference smooth wall case (case SW in table 1) is also included in this study for comparison at the same freestream velocity and measurement plane. For this case, δ_s corresponds to 98% of smooth wall boundary layer thickness. The parameters of the experiments are detailed in figure 1(a). The measurement plane is illuminated by a laser sheet generated from an InnoLas SpitLight Compact PIV 400 dual pulse Nd:YAG laser and a typical optical configuration. The thickness of the laser sheet is estimated using a method described in Grayson et al. (2018). The freestream velocity of the tunnel is maintained at $U_\infty \approx 15$ ms^{-1} for all cases, which corresponds to $Re_x \approx 4 \times 10^6$, and flow is seeded with polyamide particles of 1–2 µm diameter.

Two 14-bit pco.4000 cameras, each equipped with a Tamron 180 mm macro lens and Scheimpflug adapter, are positioned upstream and downstream of the measurement plane to capture the PIV images, as shown in figure 1. The cameras are angled about $\pm 40°$ with respect to the freestream. As many as 4800 image pairs are captured for each spanwise heterogeneneous case in table 1, while only

1200 pairs are captured for case SW. Image pairs are acquired at at a frame rate of 1 Hz, which corresponds to the boundary layer turnover rate of $TU_\infty/\delta_s = 270$ for case SW. The timing between two images is $\Delta t = 85$ µs ($t^+ = 1.7$ for case SW). The FOV width is 0.24 m or $\geq 2S$ for SR25, SR50, and SR100, but $< 2S$ for case SR160 and SR250. For these latter two cases, the FOV is limited to the region close to the rough-to-smooth interface and a complete pair of roll modes may not be captured for these cases.

Stereoscopic calibration is performed by capturing images of a two-sided calibration target at 9 streamwise locations with a distance of 500 µm between each location. This calibration target has a laser etched regular grid of dots with a 3 mm dot diameter and 10 mm spacing in the y and z direction. The self-calibration technique (Wieneke, 2005; Rama Reddy et al., 2016) is employed to obtain the calibration matrix and to correct slight misalignments between the image plane and the calibration target. In the present self-calibration algorithm, a pinhole camera model is assumed and the misalignments are calculated from the particle image disparity map between the two cameras.

The cross-correlation of image pairs and post-processing of the resulting vectors are performed using an in-house PIV package developed at the University of Melbourne (de Silva et al., 2014). Velocity vectors are reconstructed from the pixel displacement vectors using the method described in Willert (1997).

MEAN FLOW FIELD

Figure 2 shows the time-averaged streamwise velocity U of three select cases, which represent $S/\overline{\delta} \gg 1$, ≈ 1, and $\ll 1$. At the largest $S/\overline{\delta}$ (case SR250, $S/\overline{\delta} = 3.63$), figure 2(a) shows that the local boundary layer is thicker above the rough than the smooth patch; this is consistent with observations from either a homogeneous rough or smooth wall flow at a matched freestream velocity. The large-scale secondary flow is shown as a bump in the mean streamwise velocity contours near the rough-to-smooth interface ($-0.5 \lesssim y/S \lesssim -0.2$), with $y = 0$ is centered on the smooth patch. Here, the common flow up occurs above the smooth patch. Since the size of the secondary flow is limited by the boundary layer at this $S/\overline{\delta}$, the relatively horizontal iso-contours of U for $y/S \gtrsim -0.2$, indicates that the flow becomes locally homogeneous. Similar behavior is also ex-
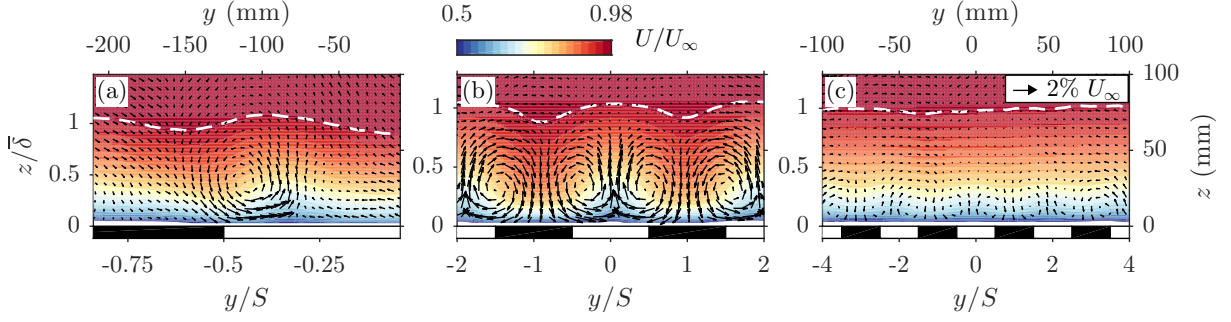
Figure 2. Contours of mean streamwise velocity U for cases (a) SR250 ($S/\overline{\delta} = 3.63$), (b) SR50 ($S/\overline{\delta} = 0.62$), (c) SR25 ($S/\overline{\delta} = 0.32$). Vectors indicate V and W, downsampled for clarity. White dashed lines are the 98% boundary layer thickness as a function of spanwise location, $\delta(y)$.
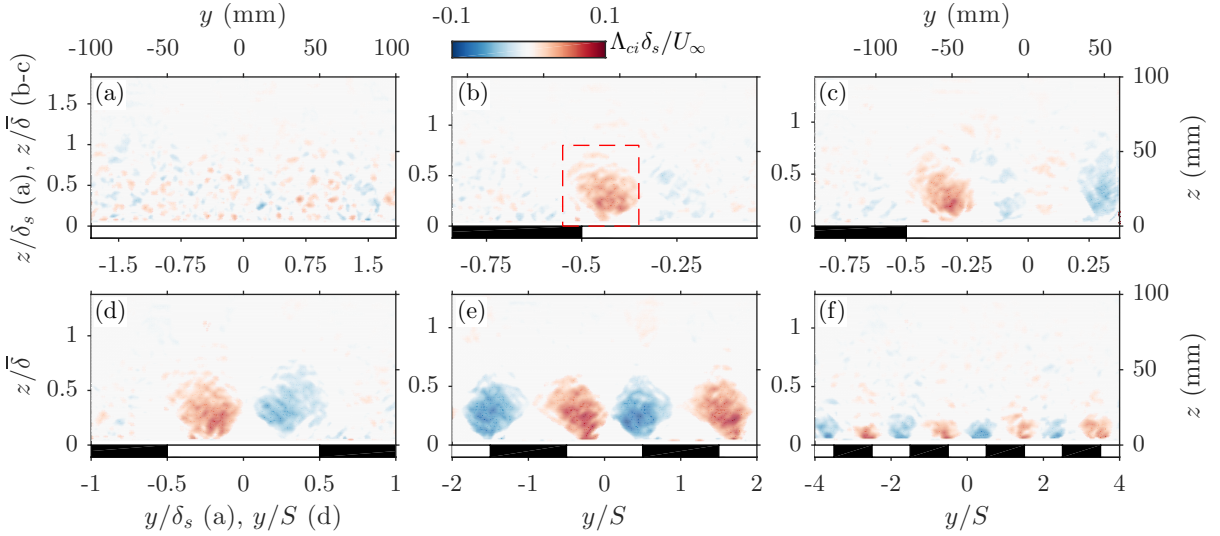

Figure 3. Large-scale secondary flows shown by the mean swirl strength multiplied by the sign of vorticity Λ_{ci} for cases (a) SW ($S/\delta_s = 0$), (b) SR250 ($S/\overline{\delta} = 3.63$), (c) SR160 ($S/\overline{\delta} = 2.28$), (d) SR100 ($S/\overline{\delta} = 1.35$), (e) SR50 ($S/\overline{\delta} = 0.62$), and (f) SR25 ($S/\overline{\delta} = 0.32$). Red indicates counterclockwise (CCW) roll modes, blue indicates clockwise (CW) roll modes. In (b), - - - illustrates the area of integration in equation 1.

pected on the rough patch further away from the interface ($y/S \lesssim -0.8$).

The case when $s/\overline{\delta} \approx 1$ (SR50) is presented in figure 2(b). Here, in terms of isocontours of streamwise velocity, we observe the reversal from cases where $S/\overline{\delta} \gg 1$; the local boundary layer is now thicker above the smooth patch due to the secondary flows, which fill the entire boundary layer. Common flow up (down) is observed above the center of the smooth (rough) patch.

The smallest $S/\overline{\delta}$ (SR25, figure 2c), where $S/\overline{\delta} \ll 1$, shows that U is nearly spanwise homogeneous, i.e. the isocontours of U flattens across the span in the wake region of the boundary layer. Here, the penetration of the secondary flow is limited by the width S and for wall-normal locations beyond the secondary flow ($z/\overline{\delta} \geq 0.32$), the flow statistics indicate spanwise homogeneity.

The vectors of mean spanwise (V) and wall-normal (W) velocity component in figure 2 illustrates the secondary flows for three $S/\overline{\delta}$ cases. Figure 3 shows the swirl strength Λ_{ci} for all of the cases in table 1 normalized by freestream velocity and SW boundary layer thickness U_∞/δ_s. The swirl is defined as the imaginary part of the complex eigenvalue of the mean velocity gradient tensor. The direction of the secondary flow, either clockwise (CW) or counterclockwise (CCW), is obtained by multiplying the swirl strength by the

sign of vorticity. Of all the cases shown in figure 3, the swirl is the strongest at SR50 (figure 3b, $S/\overline{\delta} \approx 1$), then it decays in strength and size as $S/\overline{\delta}$ decreases further to SR25 (figure 3c, $S/\overline{\delta} \ll 1$). In this case, where there is very little variation in virtual origin between the rough and smooth patches, we observe no reversal in the sign of the secondary flows at $S/\overline{\delta} \approx 1$ as suggested by Yang & Anderson (2018).

The trend of the swirl strength for all $S/\overline{\delta}$ cases is shown in figure 4(a). The plot is obtained by integrating Λ_{ci} across the spanwise location of the large-scale secondary flow, $y_{sc} - D/2 \leq y \leq y_{sc} + D/2$, and the wall-normal location, $0 < z \leq D$, both obtained from PIV results in figure 3,

$$I_{\Lambda_{ci}} = \frac{1}{N} \sum^{N} \frac{1}{A} \int_{0}^{D} \int_{y_{sc}-D/2}^{y_{sc}+D/2} \left| \frac{\Lambda_{ci}\delta_s}{U_\infty} \right| dy\, dz \qquad (1)$$

where y_{sc} is the spanwise location of the secondary flow, D is the diameter of the secondary flow, and A is the area of integration, as shown in figure 3. For cases where a number (N) of roll modes are present in the FOV (cases SR25 and SR50), the integrated Λ_{ci} is averaged over N. For the reference SW case ($S/\delta_s = 0$), Λ_{ci} is integrated over the entire
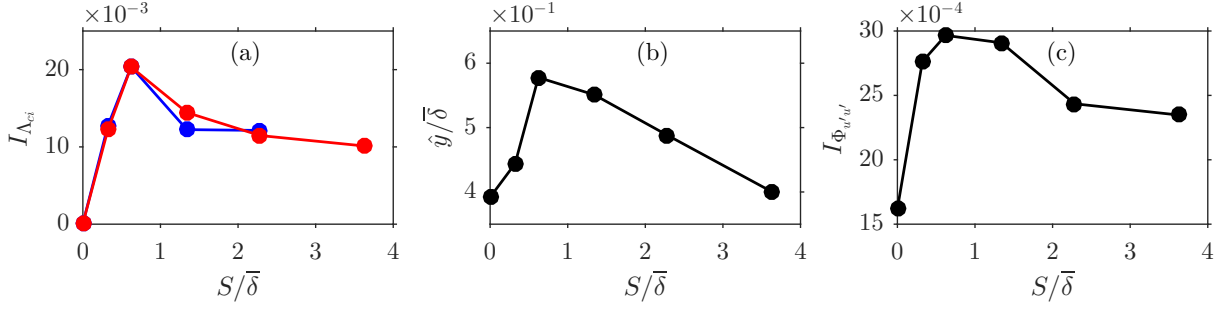
3

Figure 4. Plot of (a) integrated swirl strength $I_{\Lambda_{ci}}$, (b) spanwise distance between conditioned correlation maps $\hat{y}/\overline{\delta}$, and (c) integrated streamwise energy spectra $I_{\Phi_{u'u'}}$, as functions of $S/\overline{\delta}$. In (a), $I_{\Lambda_{ci}}$ of counterclockwise (—●—) and clockwise (—●—) roll modes inside the FOV (if any).

FOV, $-2\delta_s \leq y \leq 2\delta_s$ and $0 \leq z \leq \delta_s$, yielding an integrated swirl strength $I_{\Lambda_{ci}}$ close to zero.

The integrated swirl strength $I_{\Lambda_{ci}}$ as a function of $S/\overline{\delta}$ in figure 4(a) confirms what is observed in figure 3. $I_{\Lambda_{ci}}$ is close to zero over a smooth wall (case SW), peaks when $S/\overline{\delta} \approx 1$, and decays as $S/\overline{\delta}$ increases further.

INSTANTANEOUS FLOW FIELD

We examine the behaviour of large-scale secondary flows in the instantaneous velocity field using the two-point correlations of streamwise velocity fluctuations u'. Here, u' is defined as the turbulent fluctuations about the wall-normal and spanwise varying mean streamwise velocity U, as shown previously in figure 2. The velocity field is filtered with a box filter of $0.1\delta_s \times 0.1\delta_s$ size for SW and $0.1\overline{\delta} \times 0.1\overline{\delta}$ for SR cases. Figure 5 shows maps of normalized correlation coefficient for filtered streamwise velocity fluctuations $R_{u'_f u'_f}$ conditioned on low-speed events $u'_f < 0$, where u'_f is the filtered streamwise velocity fluctuations. The fraction of $u'_f < 0$ events is about 50% of all images, for all cases. Two-point correlations are taken at reference wall-height $z_{ref}/\delta_s = 0.1$ for SW and $z_{ref}/\overline{\delta} = 0.1$ for SR cases. We consider the correlation maps in figure 5 as a representation of a low-speed structure ($R_{u'_f u'_f} > 0$) flanked by two high-speed structures ($R_{u'_f u'_f} < 0$).

The filled contours in figure 5(a) shows the correlation map of the smooth wall case. Here, the flow is homogeneous in the spanwise direction and the conditional averaging is taken at every low-speed event occurring at the wall-height reference $z_{ref}/\delta_s = 0.1$. The same spanwise heterogeneous roughness cases as in figure 2 are also shown to represent the three limiting cases: SR250 (figure 5b–d, $S/\overline{\delta} \gg 1$), SR50 (figure 5e–g, $S/\overline{\delta} \approx 1$), and SR25 (figure 5h–j, $S/\overline{\delta} \ll 1$). The flow is heterogeneous in the spanwise direction, hence we choose three different spanwise locations y_{ref} for conditional averaging. These locations are related to the occurrence of large-scale secondary flow as illustrated in figure 3: the common flow up (figure 5b, e, h), the center of a roll mode (figure 5c, f, i), and the common flow down (figure 5d, g, j).

For the common flow up regions, the positive correlation maps $R_{u'_f u'_f} > 0$ in figure 5 (red filled contours) do not show a marked difference between the smooth wall (figure 5a) and heterogeneous case (figure 5b, e, h), except for the height of the correlation maps. The wall-normal height in mm of the $R_{u'_f u'_f} > 0$ contours in all SR cases is taller than that in the SW case; this is expected since the pres-

ence of large-scale secondary flows in SR cases increases the local boundary layer thickness in the common flow up regions and thus the structures scale accordingly. It should be noted that all plots in figure 5 are shown with the same spatial extent (see ordinate and abscissa on the right hand side and top).

The maps of $R_{u'_f u'_f} > 0$ over the center of a roll mode are shown in figure 5(c, f, i). Conditional averaging is taken over the center of a counterclockwise roll mode. Corresponding conditional averages for clockwise roll modes are not shown since they mirror the counterclockwise calculations. Here, the regions of $R_{u'_f u'_f} > 0$ (red filled contours) are typically inclined to the left. The inclination to the left hints at how a CCW secondary flow affects the streamwise alignment of large-scale structures. We observe a dependency in the inclination with the spanwise wavelength of heterogeneity. The correlation map leans strongly for case SR50 (figure 5f, $S/\overline{\delta} \approx 1$) and less so for case SR250 (figure 5c, $S/\overline{\delta} \gg 1$) and SR25 (figure 5i, $S/\overline{\delta} \ll 1$).

The maps of $R_{u'_f u'_f} > 0$ over the common flow down are shown in figure 5(d, g, j). The correlation map in SR250 (figure 5d) and especially SR50 (figure 5g) are shorter and wider than those above the common flow up. This is a result of the common flow down tendency in this region, giving way to spanwise diverging flows as the wall is approached. A less stark difference is observed in the correlation map of case SR25 in terms of leaning tendency (figure 5i) and correlation map height (figure 5j), which perhaps is the further evidence of the decaying size (and effect) of the secondary flows as the surface approaches spanwise homogeneity for this $S/\overline{\delta}$ range.

A condition for filtered spanwise velocity fluctuation v'_f is added to the two-point correlation calculations to further examine the leaning tendency of the large-scale structures. Here, v'_f filtered with a box filter of $0.1\delta_s \times 0.1\delta_s$ size for SW and $0.1\overline{\delta} \times 0.1\overline{\delta}$ for SR cases. This additional condition is met in approximately 25% of all images (for $u'_f < 0$ events that are accompanied by large-scale negative spanwise velocity component $v'_f < 0$) and a further 25% of images exhibiting $u'_f < 0$ accompanied by $v'_f > 0$. Solid red and blue contour lines in figure 5 are the correlation maps under positive and negative v'_f condition, respectively, shown only at $R_{u'_f u'_f} = 0.1$ for clarity. The conditional structure leans right and left for all SW and SR cases in figure 5 irrespective of spanwise conditioning location. A more pronounced leaning is exhibited over the common flow up (figure 5b, e, h) regions, particularly in case SR50 (figure 5e). Similar behaviour is observed in Kevin et al. (2017) over
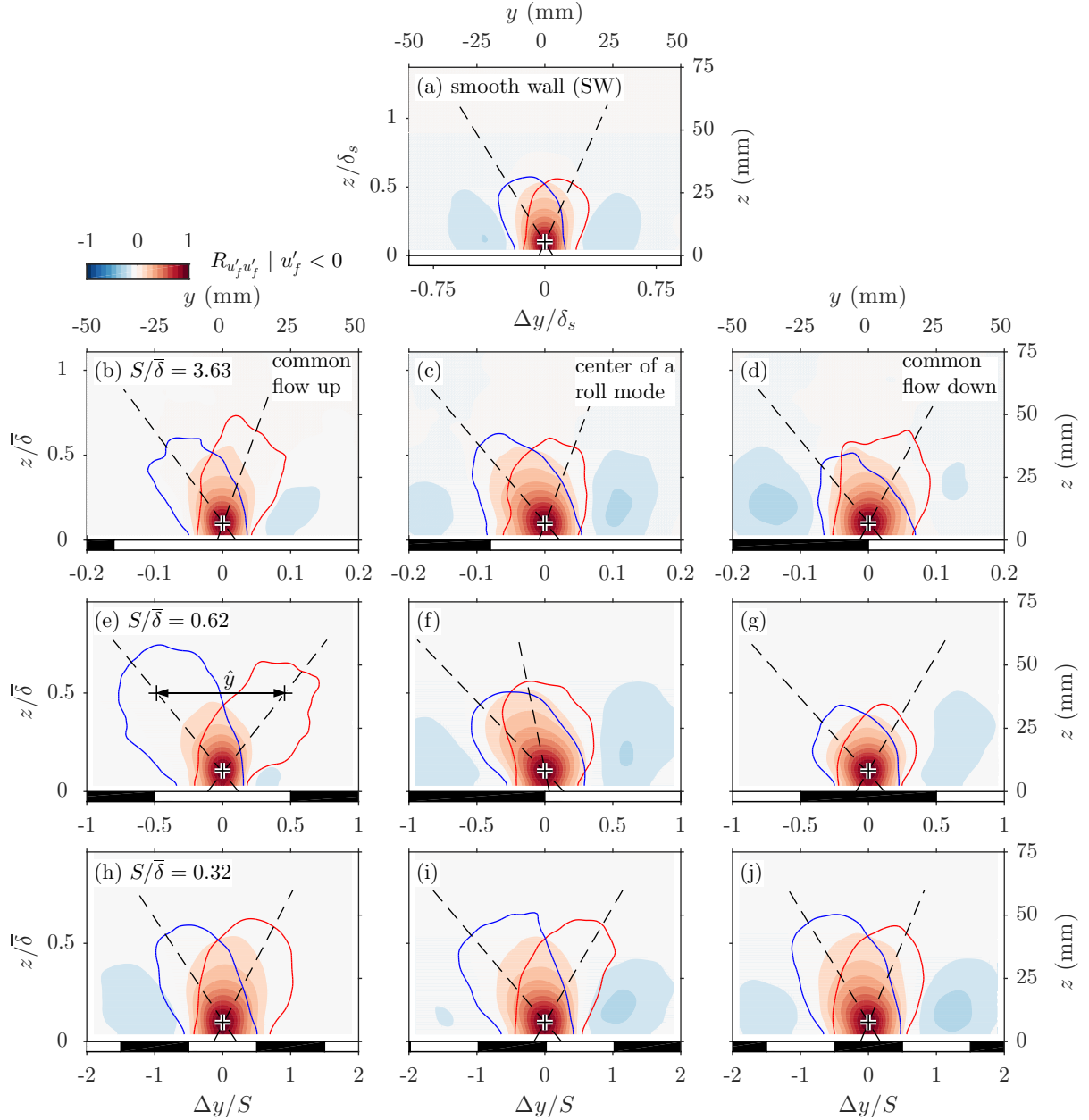
Figure 5.   Contour of normalized two-point correlation coefficient $R_{u'_f u'_f}$ at low speed event $u'_f < 0$ for case (a) SW ($S/\overline{\delta} = 0$), (b–d) SR250 ($S/\overline{\delta} = 3.63$), (e–g) SR50 ($S/\overline{\delta} = 0.62$), and (h–j) SR25 ($S/\overline{\delta} = 0.32$). Conditional averaging for SR cases is taken at three spanwise locations: common flow up (b, e, h), center of a roll mode (c, f, i), common flow down (d, g, j) . '+' symbol indicates the reference wall-height point at $z_{ref}/\delta_s = 0.1$ (a) and $z_{ref}/\overline{\delta} = 0.1$ (b–j). Red and blue solid contour lines are $R_{u'_f u'_f} = 0.1$, conditioned based on the sign of the spanwise velocity fluctuations: $v'_f > 0$ (——) and $v'_f < 0$ (——). Dashed line (- - -) shows the inclination of the conditioned correlation maps. In (e), $\hat{y}$ is the distance between v'_f-conditioned correlation maps measured at $z/\overline{\delta} = 0.5$.

the converging region of converging-diverging riblets where $S/\delta \approx 1$.

We quantify the leaning tendency by measuring the spanwise distance $\hat{y}$ between the positive and negative v'_f-conditioned correlation contours over the common flow up at a certain wall-height. The dashed lines in figure 5 show the major axis of the v'_f conditioned correlation contours, drawn by taking the linear trend of maximum $R_{u'_f u'_f}$ at every wall-normal location. Spanwise distance $\hat{y}$ is measured at $y/\delta_s = 0.5$ for SW and $y/\overline{\delta} = 0.5$ for SR cases. A visual representation showing the extraction of $\hat{y}$ from the conditional correlation maps is shown in figure 5(e). The plot of

$\hat{y}$ as a function of $S/\overline{\delta}$ over the common flow up is shown in figure 4(b). A clear peak in this leaning tendency is observed for $S/\overline{\delta} \approx 1$. This is a similar spanwise wavelength to that at which the strongest roll-modes are observed in figure 4(a).

The leaning tendency of large-scale structures for the SR cases can be interpreted as time-varying behaviour of the secondary flows since the condition vector v'_f is a time-varying signal. The particularly strong leaning tendency when $S/\overline{\delta} \approx 1$ suggests that the time-varying behaviour of the secondary flows is particularly pronounced at certain heterogeneous wavelengths. Previous clues to this be-

haviour have been provided by 1-D streamwise energy spectrograms acquired with hot-wire anemometry (HWA) measurements by Wangsawijaya *et al.* (2018) over the same surfaces. There, measurements were performed over a spanwise-wall-normal grid spanning one half-wavelength S over the same set of heterogeneous surfaces. A pronounced peak in the premultiplied streamwise energy spectra $k_x\Phi_{u'u'}$ (where k_x is the streamwise wavenumber) has been observed for surfaces where $S/\overline{\delta} \approx 1$. As with the previous discussions, we quantify the strength of this emergent peak in the energy spectrum by integrating the HWA-acquired $k_x\Phi_{u'u'}$ over all resolved k_x, wall-normal locations $(0 < z \le \overline{\delta})$, and a spanwise length about the location of the secondary flow where the spectral peak is observed $(y_{sc} - D/4 \le y \le y_{sc} + D/4)$,

$$ I_{\Phi_{u'u'}} = \frac{1}{A} \int_0^{\overline{\delta}} \int_{y_{sc}-D/4}^{y_{sc}+D/4} \int_0^\infty \frac{k_x\Phi_{u'u'}}{U_\infty^2} \mathrm{d}(\log k_x) \, \mathrm{d}y \, \mathrm{d}z \qquad (2) $$

where A is the area of integration in wall-normal and spanwise direction.

The energy integrated over a roll mode $I_{\Phi_{u'u'}}$ as a function of $S/\overline{\delta}$ is shown in figure 4(c). The trend is again similar to that observed in the swirl strength (figure 4a) and the leaning tendency in the cross-plane (figure 4b). The maximum value of $I_{\Phi_{u'u'}}$ at $S/\overline{\delta} \approx 1$ is the result of a strong emergent energy peak in the outer layer at $z/\overline{\delta} \approx 0.5$ occurring at streamwise wavelengths of $\lambda_x/\overline{\delta} = 3\text{--}4$ (Wangsawijaya *et al.*, 2018).

The outer peak suggests that instantaneously, the secondary flow meanders or fluctuates with a preferred streamwise wavelength. We can now complete our observation on the dependency of the large-scale secondary flow on $S/\overline{\delta}$. The time-averaged secondary flow is the strongest when $S/\overline{\delta} \approx 1$. For the same range of spanwise wavelengths, the secondary flows seem to be highly time-varying, exhibiting a strong meandering tendency with a preferred streamwise meandering wavelength and spanwise amplitude.

CONCLUSIONS

In this study, we conduct cross-stream plane SPIV in a turbulent boudary layer over surfaces composed of spanwise heterogeneity, where the half-wavelength S is varied in the range of $S/\overline{\delta} = 0.32\text{--}3.63$. Current results reveal that for the limiting case $S/\overline{\delta} \gg 1$, the flow becomes homogeneous with respect to its local shear stress at the regions away from the secondary flow. At the other limit where $S/\overline{\delta} \ll 1$, the flow becomes spanwise homogeneous above the near-wall region, which is unaffected by the secondary flow. On the other hand, the flow is truly spanwise heterogeneous when $S/\overline{\delta} \approx 1$, where the roll modes are the strongest compared to other limiting cases and space-filling. Further conditional averaging of filtered streamwise velocity u'_f indicates that the spanwise leaning of the large-scale structures is strongly varying with time for this same range $(S/\overline{\delta} \approx 1)$. Emergent peaks in HWA-measured spectra suggest a similar behaviour. Together these results indicate that not only do the secondary flows introduced by spanwise heterogeneous surfaces strengthen at $S/\overline{\delta} \approx 1$, but also that for this particular range of wavelengths, the secondary flows

exhibit a pronounced unsteady meandering behaviour that adds to the overall turbulence levels of the flows.

REFERENCES

Chung, D., Monty, J. P. & Hutchins, N. 2018 Similarity and structure of wall-turbulence with lateral wall shear stress variations. *J. Fluid Mech.* **847**, 591–613.

Grayson, K., de Silva, C. M., Hutchins, N. & Marusic, I. 2018 Impact of mismatched and misaligned laser light sheet profiles on PIV performance. *Exp. Fluids* **59**, 2.

Hama, F. R. 1954 Boundary-layer characteristics for rough and smooth surfaces. *Trans. SNAME* **62**, 333–351.

Hinze, J. O. 1967 Secondary currents in wall turbulence. *Phys. Fluid* **10**, S122.

Kevin, Monty, J. P., Bai, H. L., Pathikonda, G., Nugroho, B., Barros, J. M., Christensen, K. T. & Hutchins, N. 2017 Cross-stream stereoscopic particle image velocimetry of a modified turbulent boundary layer over directional surface pattern. *J. Fluid Mech.* **813**, 412–435.

Medjnoun, T., Vanderwel, C. & Ganapathisubramani, B. 2018 Characteristics of turbulent boundary layers over smooth surfaces with spanwise heterogeneity. *J. Fluid Mech.* **838**, 516–543.

Moody, L. F. 1944 Friction factors for pipe flow. *ASME Trans.* **66**, 671–684.

Nugroho, B., Hutchins, N. & Monty, J. P. 2013 Large-scale spanwise periodicity in a turbulent boundary layer induced by highly ordered and directional surface roughness. *Int. J. Heat Fluid Flow* **41**, 90–102.

Rama Reddy, G. V., Philip, J. & Marusic, I. 2016 The effects of laser-sheet misalignment on stereo-PIV measurements in wall-bounded turbulence. In *Proceedings of the 20th Australasian Fluid Mechanics Conference* (ed. G. Ivey, N. Jones & T. Zhou). Australasian Fluid Mechanics Society.

de Silva, C. M., Gnanamanickam, E. P., Atkinson, C., Buchmann, N. A., Hutchins, N., Soria, J. & Marusic, I. 2014 High spatial range velocity measurements in a high Reynolds number turbulent boundary layer. *Phys. Fluid* **26**, 025117.

Wangsawijaya, D. D., de Silva, C. M., Baidya, R., Chung, D., Marusic, I. & Hutchins, N. 2018 Secondary flow over surfaces with spanwise heterogeneity. In *Proceedings of the 21st Australasian Fluid Mechanics Conference* (ed. T. C. W. Lau & R. M. Kelso). Australasian Fluid Mechanics Society.

Wieneke, B. 2005 Stereo-PIV using self-calibration on particle images. *Exp. Fluids* **39**, 267–280.

Willert, C. 1997 Stereoscopic digital particle image velocimetry for application in wind tunnel flows. *Meas. Sci. Technol.* **8**, 1465–1479.

Yang, J. & Anderson, W. 2018 Numerical study of turbulent channel flow over surfaces with variable spanwise heterogeneities: topographically-driven secondary flows affect outer-layer similarity of turbulent length scales. *Flow Turbul. Combust.* **100** (1), 1–17.